JACS
JOURNAL OF THE AMERICAN CHEMICAL SOCIETY

Article

pubs.acs.org/JACS

Harvesting Highly Electronically Excited Energy to Triplet Manifolds: State-Dependent Intersystem Crossing Rate in Os(II) and Ag(I) Complexes

Cheng-Chih Hsu,[†] Chao-Chen Lin,[†] Pi-Tai Chou,*[,†] Chin-Hung Lai,[†,§] Chien-Wei Hsu,[‡] Chen-Huey Lin,[‡] and Yun Chi*[,‡]

[†]Department of Chemistry, National Taiwan University, No. 1, Sec. 4, Roosevelt Road, Taipei 10617, Taiwan, R.O.C.

[‡]Department of Chemistry, National Tsing Hua University, No. 101, Sec. 2, Kuang-Fu Road, Hsinchu 30013, Taiwan, R.O.C.

Supporting Information

ABSTRACT: A series of newly synthesized Os(II) and Ag(I) complexes exhibit remarkable ratiometric changes of intensity for phosphorescence versus fluorescence that are excitation wavelength dependent. This phenomenon is in stark contrast to what is commonly observed in condensed phase photophysics. While the singlet to triplet intersystem crossing (ISC) for the titled complexes is anomalously slow, approaching several hundred picoseconds in the lowest electronic excited state ($S_1 \rightarrow T_1$), higher electronic excitation leads to a much accelerated rate of ISC (10^{11}–10^{12} s^{-1}), which is competitive with internal conversion and/or vibrational relaxation, as commonly observed in heavy transition metal complexes. The mechanism is rationalized by negligible metal d orbital contribution in the S_1 state for the titled complexes. Conversely, significant ligand-to-metal charge transfer character in higher-lying excited states greatly enhances spin–orbit coupling and hence the ISC rate. The net result is to harvest high electronically excited energy toward triplet states, enhancing the phosphorescence.

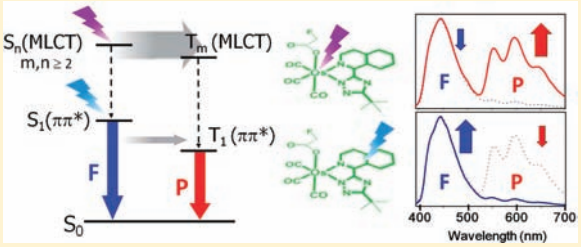

INTRODUCTION

Regardless of the excitation wavelength, it has been well established that fast internal conversion (IC) and vibrational relaxation (VR) take place in solution and in solid, such that fluorescence originates from the thermally equilibrated, lowest-lying excited singlet state S_1. For heavy transition-metal complexes, following the fast intersystem crossing (ISC) and solvent/phonon relaxation, the phosphorescence ought to stem from the lowest triplet state, T_1, in the solution/solid phase. The consequence of such a phenomenon, which is commonly referred to as "Kasha's rule",[1] proves to be unanimous and is typically reflected in the excitation wavelength independent emission spectral profile. Nevertheless, cases of $S_2 \rightarrow S_0$ fluorescence have been well-documented for carotenoids,[2] azulene,[3] and thiophosgene in the vapor phase,[4] owing to the forbidden transition of $S_1 \rightarrow S_0$ or a small Franck–Condon factor which reduces the rate of $S_2 \rightarrow S_1$ internal conversion. In addition, molecules undergoing faster photochemical reaction processes in the highly electronic excited state S_n ($n > 1$), such as the ring opening of a fluorinated indolylfulgide,[5] also demonstrate relaxation without having to populate the S_1 first. It is also noteworthy that for molecules without photochemical reaction channels, due to the congestion of states, among which some shallow or even repulsive potential energy surfaces (PESs) may couple with the ground state PES, the highly electronic excited states frequently undergo facile radiationless pathways down to the ground state. Thus, excitation to higher electronic excited states commonly contributes less to the emission and hence a decrease of intensity in the shorter wavelength region of the excitation spectrum.

The aforementioned empirical rules also apply to second- and third-row transition-metal complexes. Over the past two decades, aiming for energy conservation and low-cost clean energy, research on such complexes has aroused considerable attention due to their latent applications in phosphorescent emitters[6−9] and solar energy devices.[10,11]

In this contribution, we report the photophysical properties of a series of new Os(II) complexes bearing isoquinoline-triazolate/pyrazolate (complexes **1**–**6**, see Chart 1 for structures). These Os(II) complexes were originally designed by anchoring multiple CO ligands to the Os(II) metal center such that the Os(II) → CO back π-electron donation could further lower the Os(II) d_π (t_{2g}) energy, therefore enlarging the energy gap. Intriguingly, the lowering of the t_{2g} orbital energy and the consequent reduction of the metal-to-ligand charge transfer contribution at the lowest excited state lead to previously unrecognized features in their excited-state behavior. More specifically, we discovered remarkable changes in the intensity ratio for phosphorescence (P) versus fluorescence (F), which is strongly excitation wavelength dependent. The P/F intensity ratio can be increased by as large as 8-fold upon tuning the electronic excitation from lowest to higher lying transitions in solution as well as in the solid state. The higher

Received: November 29, 2011
Published: April 19, 2012

   dx.doi.org/10.1021/ja2107788 | J. Am. Chem. Soc. 2012, 134, 7715–7724

Chart 1. Os(II) and Ag(I) Complexes That Exhibit Excitation-Energy-Dependent Ratiometric Changes for Phosphorescence versus Fluorescence

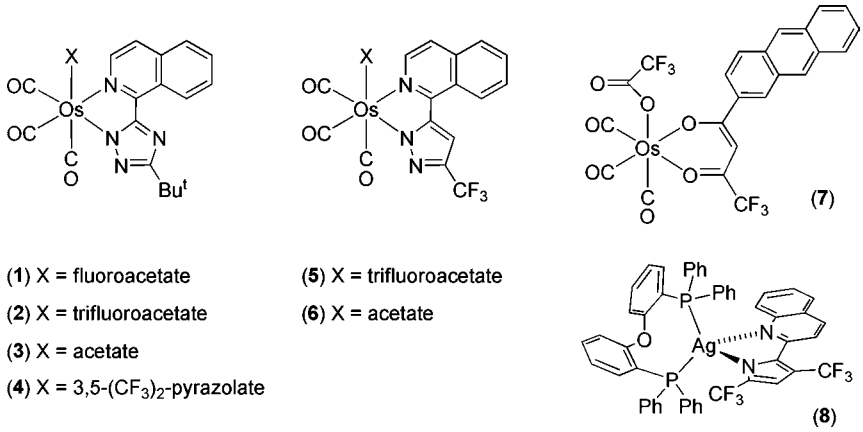

energy excitation leading to higher phosphorescence intensity ratio (versus fluorescence) is truly exceptional to most spectroscopic observations so far. Details of the syntheses, spectroscopic characterization, relaxation dynamics, and the unified theory based on DFT calculations of the proposed conversion mechanism, including the additional Ag(I) complex, are elaborated in the following sections.

EXPERIMENTAL SECTION

Synthesis and Characterization. *General Procedures.* All reactions were performed under an argon atmosphere, and solvents were distilled from appropriate drying agents prior to use. Commercially available reagents were used without further purification unless otherwise stated. All reactions were monitored using precoated TLC plates (0.20 mm with fluorescent indicator UV_{254}). Mass spectra were obtained on a JEOL SX-102A instrument operating in electron impact (EI) or fast atom bombardment (FAB) mode. ^{1}H and ^{13}C NMR spectra were recorded on a Varian Mercury-400 or an INOVA-500 instrument. Elemental analyses were conducted at the NSC Regional Instrumentation Center at National Chiao Tung University. Osmium reagent $[Os(CO)_3(tfa)_2]$ was prepared from the direct treatment of $Os_3(CO)_{12}$ with trifluoroacetic acid.[12,13] The chelating ligands, 3-*tert*-butyl-5-(1-isoquinolinyl)-1,2,4-triazole (bitzH) and 3-trifluoromethyl-5-(1-isoquinolinyl)-1,2-pyrazole (fipzH), were prepared according to the literature procedures.[14] Os(II) and Ag(I) complexes **7** and **8** were synthesized using literature procedures.[15,16]

*1. Synthesis of Os(bitz)(tfa)(CO)$_3$ (**2**).* $[Os(CO)_3(tfa)_2]$ (100 mg, 0.20 mmol) and 3-*tert*-butyl-5-(1-isoquinolinyl)-1,2,4-triazole (bitzH, 55 mg, 0.22 mmol) were refluxed in anhydrous toluene (20 mL) for three hours. After then, the solvent was removed under vacuum and residue purified using column chromatography eluting with a 1:1 mixture of ethyl acetate and hexane. Single crystals of $[Os(bitz)(tfa)(CO)_3]$ were recrystallized from a hexane solution at RT (89 mg, 0.14 mmol, 70%).

*Spectral Data of **2**.* ^{1}H NMR (500 MHz, $CDCl_3$, 298 K): δ 10.25 (d, J_{HH} = 8 Hz, 1H), 8.48 (d, J_{HH} = 6.5 Hz, 1H), 7.97−7.90 (m, 3H), 7.68 (d, J_{HH} = 6.5 Hz, 1H), 1.49 (s, 9H). ^{19}F NMR (470 MHz, $CDCl_3$, 298 K): δ −74.02 (s, 3F). IR (C_6H_{12}): ν(CO), 2127 (vs), 2057 (vs), 2030 (vs) cm^{-1}. MS (FAB, ^{192}Os): m/z 641 (M + 1)$^+$, 527 (M − tfa)$^+$. Anal. Calcd for $C_{20}H_{15}F_3N_4O_5Os$: C, 37.62; N, 8.77; H, 2.37. Found: C, 37.62; N, 8.72; H, 2.81.

*2. Synthesis of Os(bitz)(fac)(CO)$_3$ (**1**).* $[Os(bitz)(tfa)(CO)_3]$ (100 mg, 0.157 mmol) and sodium fluoroacetate (63 mg, 0.63 mmol) were refluxed in methanol (20 mL) for four hours. The solvent was removed under vacuum and residue purified using column chromatography eluting with a 1:1 mixture of ethyl acetate and hexane. Single crystals of $[Os(bitz)(fac)(CO)_3]$ were recrystallized from a hexane solution at RT (83 mg, 0.14 mmol, 89%). The bitz derivatives **3** and **4** were synthesized from **1** and sodium acetate or 3,5-bis(trifluoromethyl)pyrazole in a similar manner.

*Spectral Data of **1**.* ^{1}H NMR (500 MHz, $CDCl_3$, 298 K): δ 10.27 (d, J_{HH} = 9.5 Hz, 1H), 8.51 (d, J_{HH} = 6.5 Hz, 1H), 7.95−7.88 (m, 3H), 7.64 (d, J_{HH} = 6.5 Hz, 1H), 4.52 (dd, J_{HF} = 73 Hz, J_{HH} = 15 Hz, 1H), 4.42 (dd, J_{HF} = 73 Hz, J_{HH} = 15 Hz, 1H), 1.50 (s, 9H). ^{19}F NMR (470 MHz, $CDCl_3$, 298 K): δ −221.4 (t, J_{HF} = 50 Hz, 1F). IR (C_6H_{12}): ν(CO), 2121 (vs), 2052 (vs), 2023 (vs) cm^{-1}. MS (FAB, ^{192}Os): m/z 604 (M)$^+$, 527 (M − fac)$^+$. Anal. Calcd for $C_{20}H_{17}FN_4O_5Os$: C, 39.86; N, 9.30; H, 2.84. Found: C, 40.31; N, 9.29; H, 3.52.

*Spectral Data of **3**.* ^{1}H NMR (400 MHz, d_6-acetone, 298 K): δ 10.28 (d, J_{HH} = 8.0 Hz, 1H), 8.82 (d, J_{HH} = 6.4 Hz, 1H), 8.17 (d, J_{HH} = 8.0 Hz, 1H), 8.05 (m, 1H), 8.00−7.96 (m, 2H), 1.63 (s, 3H), 1.47 (s, 9H). IR (C_6H_{12}): ν(CO), 2117 (vs), 2050 (vs), 2019 (vs) cm^{-1}. MS (FAB, ^{192}Os): m/z 587 (M + 1)$^+$, 527 (M − ac)$^+$. Anal. Calcd for $C_{20}H_{18}N_4O_5Os$: C, 41.09; N, 9.58; H, 3.10. Found: C, 41.11; N, 9.76; H, 3.34.

*Spectral Data of **4**.* ^{1}H NMR (400 MHz, $CDCl_3$, 298 K): δ 10.15 (d, J_{HH} = 8.0 Hz, 1H), 8.73 (d, J_{HH} = 6.8 Hz, 1H), 7.87−7.79 (m, 3H), 7.65 (d, J_{HH} = 6.8 Hz, 1H), 6.41 (s, 1H), 1.49 (s, 9H). IR (C_6H_{12}): ν(CO), 2126 (vs), 2057 (vs), 2040 (vs) cm^{-1}. MS (FAB, ^{192}Os): m/z 730 (M)$^+$, 528 (M − tfpz)$^+$ Anal. Calcd for $C_{23}H_{16}F_6N_6O_3Os$: C, 37.91; N, 11.53; H, 2.21. Found: C, 37.93; N, 11.23; H, 2.46.

*3. Synthesis of Os(fipz)(tfa)(CO)$_3$ (**5**).* $[Os(CO)_3(tfa)_2]$ (100 mg, 0.20 mmol) and 3-trifluoromethyl-5-(1-isoquinolinyl)-1,2-pyrazole (fipzH, 27 mg, 0.103 mmol) were refluxed in anhydrous toluene (10 mL) for three hours. After then, the solvent was removed under vacuum and residue purified using column chromatography eluting with a 1:1 mixture of ethyl acetate and hexane. Crystalline samples were obtained from a hexane solution at RT (59 mg, 0.090 mmol, 91%).

*Spectral Data of **5**.* ^{1}H NMR (500 MHz, d_6-acetone, 298 K): δ 9.08 (d, J_{HH} = 8.0 Hz, 1H), 8.97 (d, J_{HH} = 6.5 Hz, 1H), 8.22 (d, J_{HH} = 8.5 Hz, 1H), 8.10−7.97 (m, 3H), 7.84 (s, 1H). ^{19}F NMR (470 MHz, d_6-acetone, 298 K): δ −61.37 (s, 3F), −74.81 (s, 3F). IR (C_6H_{12}): ν(CO), 2129 (vs), 2059 (vs), 2032 (vs) cm^{-1}. MS (FAB, ^{192}Os): m/z 652 (M + 1)$^+$, 538 (M − tfa)$^+$. Anal. Calcd for $C_{18}H_7F_6N_3O_5Os$: C, 33.29; N, 6.47; H, 1.09. Found: C, 33.13; N, 6.49; H, 1.49.

*4. Synthesis of Os(fipz)(ac)(CO)$_3$ (**6**).* The acetate derivative complex (**6**) was synthesized from **5** and sodium acetate in 91% yield.

*Spectral Data of **6**.* ^{1}H NMR (500 MHz, d_6-acetone, 298 K): δ 9.07 (d, J_{HH} = 8.5 Hz, 1H), 8.87 (d, J_{HH} = 6.5 Hz, 1H), 8.21 (d, J_{HH} = 8.0 Hz, 1H), 8.06 (t, J_{HH} = 7.6 Hz, 1H), 8.00−7.96 (m, 2H), 7.81 (s, 1H), 1.63 (s, 3H). ^{19}F NMR (470 MHz, d_6-acetone, 298 K): δ −61.19 (s, 3F). IR (C_6H_{12}): ν(CO), 2119 (vs), 2052 (vs), 2021 (vs) cm^{-1}. MS (FAB, ^{192}Os): m/z 598 (M + 1)$^+$, 538 (M − ac)$^+$. Anal. Calcd for $C_{18}H_{10}F_3N_3O_5Os$: C, 36.30; N, 7.06; H, 1.69. Found: C, 35.66; N, 6.79; H, 2.04.

Spectroscopy and Dynamics Measurements. Steady state absorption and emission spectra were recorded by a Hitachi (U-3310)

dx.doi.org/10.1021/ja2107788 | J. Am. Chem. Soc. 2012, 134, 7715−7724

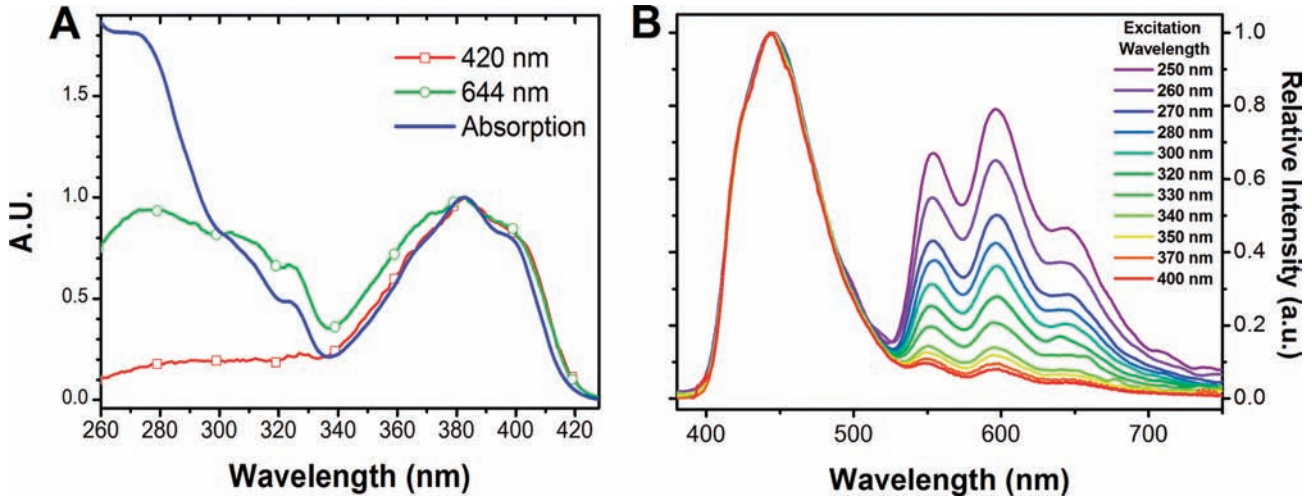

Figure 1. Steady state spectra of complex **1** in aerated CH_2Cl_2 at 298 K. (A) Normalized absorption and excitation spectra monitored at different emission wavelengths. The excitation spectrum monitored at 420 nm (-□-) reveals a deficiency of constitution at short wavelengths as compared to those measured at 644 nm (-O-) and steady state absorption (−). (B) Excitation-wavelength-dependent (250−400 nm) emission spectra normalized at the fluorescence peak maxima. The intensity ratio for phosphorescence versus fluorescence increases by about 8 times while tuning λ_{ex} from 400 to 250 nm.

Table 1. Photophysical Properties for Os(II) Complexes 1−6

	UV/vis [nm] ($M^{-1}\cdot cm^{-1}$)	PL λ_{max} [nm]	[a]Φ [%] (long λ_{ex})	[b]Φ [%] (short λ_{ex})	[c]τ (ps) = θ_{isc}/k_{isc}	[d]τ* (ps) ≈ θ_{hisc}/k_{hisc}	[a]τ_p (μs)	[e]θ_{hisc} [%]	k_{isc} (s^{-1})	[e]k_{hisc} (s^{-1})
1	384 (13783)	444, 597	1.39, 25.61	0.09, 8.43	96.5	1.1	61.2	6.8	2.65×10^9	6.2×10^{10}
2	386 (11400)	446, 598	2.56, 23.37	0.12, 5.58	111.1	1.2	51.7	4.5	2.10×10^9	3.7×10^{10}
3	383 (8338)	445, 597	0.91, 28.51	0.06, 9.93	55.1	1.5	81.8	8.1	5.17×10^9	5.4×10^{10}
4	385 (9586)	444, 598	1.42, 26.82	0.10, 9.69	64.7	1.1	106.0	7.8	4.15×10^9	7.1×10^{10}
5	371 (12421)	422, 589	0.48, 18.83	0.05, 6.52	22.1	0.7	129.7	4.6	8.52×10^9	6.5×10^{10}
6	369 (10503)	417, 585	0.13, 19.20	0.01, 4.05	5.6	0.6	141.8	2.6	3.43×10^{10}	4.3×10^{10}

[a]Data were recorded in degassed CH_2Cl_2 solution at room temperature with λ_{ex} = 400 nm for **1**−**4** and 390 nm for **5**−**6**. [b]And with λ_{ex} = 266 nm for all complexes. Φ values for fluorescence were listed in front, in accordance with the order of λ_{max}. Note that Φ for phosphorescence, in this context, is equal to θ_{isc} for **1**−**6**. [c]Data were recorded via femto−picosecond transient absorption in aerated CH_2Cl_2 solution at room temperature with λ_{ex} = 400 nm for **1**−**4** and 390 nm for **5**−**6**. [d]And with λ_{ex} = 266 nm for all complexes. [e]Estimated for λ_{ex} = 266 nm.

spectrophotometer and an Edinburgh (FS920) fluorometer with corrected emission and excitation profiles, respectively. Phosphorescence lifetime measurements were performed with an Edinburgh FL 900 photon-counting system.

Nanosecond transient absorption was recorded with a laser flash photolysis system (Edinburgh LP920), in which the third harmonic (355 nm, fwhm ~8 ns) of an Nd:YAG laser (Continuum Surelite) and a white light square pulse were used as the pump and probe beams, respectively. These two pulses were crossed at a 90° angle with an overlapping distance of 10 mm. The temporal resolution was limited by the excitation pulse duration of approximately 10 ns. A quartz cuvette sample (1.0 cm in width) containing solution of ~4 mL was used in the nanosecond transient absorption experiments.

The femtosecond transient absorption measurements were performed according to the previous report.[17] Briefly, a regenerative amplifier (Spitfire Pro, Spectra Physics) seeded by a mode-locked Ti:sapphire laser (Tsunami, Spectra Physics) was used as the laser source. The output of the system consists of pulses of 800 or 780 nm, 1 W, 150 fs (fwhm), at a repetition rate of 1 kHz. The pump−probe spectroscopic setup was based on an ExciPro spectrometer (CDP System Corp, maximum delay time 2 ns for the double pass configuration). For 400 or 380 nm excitation, the laser output was passed through a 0.5 mm thick β-BaB_2O_4 crystal to generate the second harmonics. For 266 nm excitation, the third harmonics of the regenerative amplifier output was employed. After separation by a dichroic mirror, the remaining laser fundamental was focused onto a 1 mm thick sapphire plate to generate the white light continuum (WLC) (450−1000 nm). After passing through the sample cell, the WLC was coupled into a 100 μm optical fiber connected to a diode array. The sample cell was a 1 mm optical path quartz cylindrical cell placed in a variable speed rotating holder or a flow system for 266 nm excitation. Typically, time-resolved absorption difference spectra were acquired averaging over 200 excitation pulses at each delay time. The overall time resolution of the system was ~200 fs. For 350 nm excitation, a traveling-wave optical parametric amplifier of white-light continuum (TOPAS-C, Spectra Physics) was driven by the 800 nm fundamental of the regenerative amplifier. The NIR signal beam (1150−1560 nm, 1kHz, 80 μJ) of TOPAS-C output was selected at 1400 nm to produce fourth harmonic (350 nm) as the pump source, and the WLC probe was produced by the residual fundamental.

Picosecond time-correlated single-photon counting (TCSPC) experiments were also performed to resolve the fluorescence decay dynamics. To avoid the saturation of triple state population, the regenerative amplifier output with kHz repetition rate was used to derive the excitation pulses. Lifetime measurements were performed using Edinburgh OB 900L as the detecting system. A polarizer was placed in the emission path to ensure that the polarization of the fluorescence was set at the magic angle (54.7°) with respect to that of the pump laser to eliminate fluorescence anisotropy. The fluorescence decays were analyzed by the sum of exponential functions with an iterative convolution method which allowed partial removal of the instrument time broadening and consequently rendered a temporal resolution of ~30 ps.

Computational Methodology. The hybrid DFT functional B3LYP is performed to optimize the geometries of **1**−**6**.[18] The 6-31G* basis set is chosen for the other elements except osmium.[19] For

dx.doi.org/10.1021/ja2107788 | J. Am. Chem. Soc. 2012, 134, 7715−7724

both osmium and Ag ions, the LANL2 ECP is applied to describe the relativistic effect, which is combined with a double-ζ basis set, i.e., LANL2DZ.[20] After obtaining the converged geometries, the vibrational frequency analyses and the time-dependent B3LYP functional are then performed to confirm the number of imaginary frequency to be zero, followed by the calculation of vertical excitation energies for each state.[21] Calculation of complex **7** has been performed in the previous work.[15] We also recognize that the parameters used do not act exactly the same way on different classes of excited states, e.g., MLCT or $\pi\pi^*$. Alternatively, the ab initio approach taking into account the electronic relaxation in the various excited states may provide a better solution.[22] However, at the current stage, it is not feasible to perform optimization at each excited state on the titled transition-metal complexes having a complicated structure. Also, the involvement of triplet states results in high density of states and hence extensive state mixing, which makes the calculation formidable. Therefore, in this theoretical approach, we hope only to qualitatively describe the trend for the percentages of MLCT/LMCT contributions, to gain insight into the underlying photophysics and to complement the experimental observations.

RESULTS AND DISCUSSION

Using complex **1** as a paradigm, Figure 1A reveals the absorption spectrum maximized at ~384 nm. Upon electronic excitation, dual emission is clearly resolved in CH_2Cl_2, which consists of a short-wavelength band (the F band) and a long-wavelength band (the P band) maximized at 445 nm (population decay time τ_f = 96.5 ± 0.5 ps) and 597 nm (τ_p = 61.2 μs in degassed and ~850 ns in aerated CH_2Cl_2), respectively (see Table 1). The assignment of F and P bands is unambiguous, considering the radiative decay rate constant (k_r) of 1.4×10^8 s^{-1} calculated for the F band and that the P band is subject to drastic O_2 quenching. Similar dual emission was resolved for all complexes **2**–**6** (Figure 2). As shown in Figure

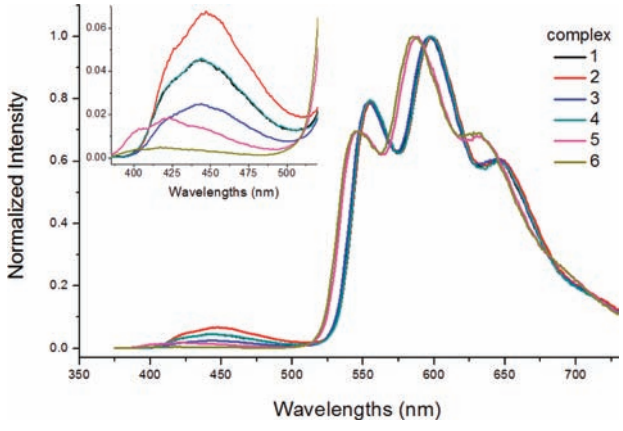

Figure 2. Normalized emission spectra for complexes **1**–**6** upon excitation at 375 nm. Notice that both the fluorescence and phosphorescence λ_{max} are blue-shifted 20 nm for **5** and **6**. Upper left: enlarged fluorescence spectra. Solution: degassed CH_2Cl_2. Temperature: 298 K.

1B and Figure S1 (Supporting Information), the most striking feature is that the intensity ratio for phosphorescence versus fluorescence is notably excitation wavelength dependent in both aerated and degassed environments (see Supporting Information Table S1 for the absolute emission quantum yields and fluorescence-to-phosphorescence ratios at various excitation wavelengths), and a similar excitation-dependent emission pattern is observed in the solid state as well (see Supporting Information, Figure S2). This unprecedented phenomenon is also reflected in the very different excitation spectra monitored for the two emission bands recorded with a calibrated fluorometer (see Figure 1A). Upon monitoring at the F band, there is a clear deficit in the shorter-wavelength region (<340 nm) compared to that monitored at the P band and the absorption spectrum, signifying that higher-energy excitation contributes more to phosphorescence.

The above-mentioned difference in the excitation spectrum, by conventional wisdom, might be promptly ascribed to trace impurities that give rise to interfering emissions. After exhaustive purification of the samples, the spectral profiles remained unchanged, eliminating the possibility that the discrepancy was caused by trace impurities. Also, similar phenomena, i.e., differences in excitation spectra upon monitoring at F and P bands, were observed in all the remaining complexes **2**–**6**, as shown in Figure 3. Moreover,

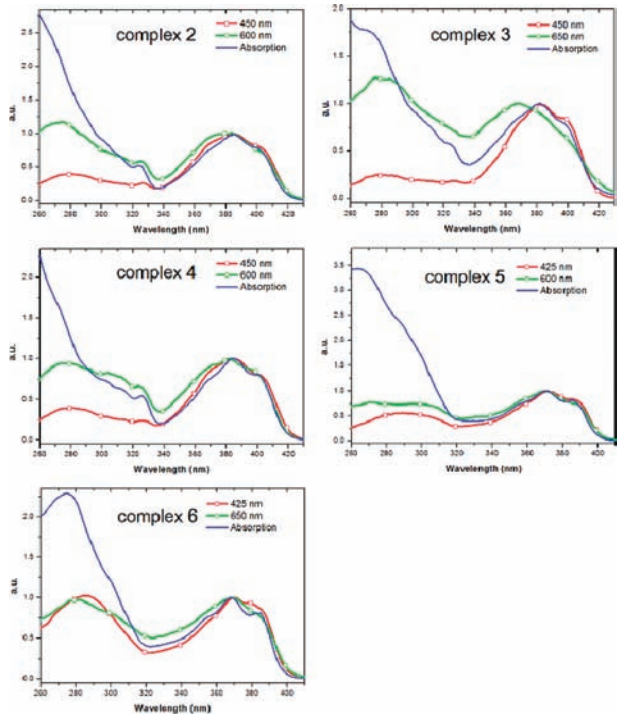

Figure 3. Normalized excitation spectra for complexes **2**–**6** monitored at different wavelengths. The spectra for each complex monitored at fluorescence wavelengths (–□–) reveal deficiencies of constitution at short excitation wavelengths as compared to those measured at phosphorescence wavelengths (–○–) and steady state absorption (–). Solution: aerated CH_2Cl_2 for complexes **2**–**6**. Temperature: 298 K.

despite the difference in the higher-energy region, the excitation spectrum in the lowest-lying state is similar for both F and P bands. Most decisively, as supported by the relaxation dynamics in the following sections, a precursor–successor relation holds firmly for F and P bands. We thus conclude that the result is genuine and is opposed to conventional observations in the condensed phase.

To rationalize the above results, an unconventional relaxation mechanism incorporating two interrelated processes is thus proposed: (1) In certain higher-lying electronic excited states (S_n ($n > 1$)) or the vibrationally excited S_1 state ($v > 0$), complex **1**, for instance, executes a faster rate of S_n ($n > 1$) → T_m ($m \geq 1$) or S_1 ($v > 0$) → T_m intersystem crossing, denoted

dx.doi.org/10.1021/ja2107788 | J. Am. Chem. Soc. 2012, 134, 7715–7724

as hyper-intersystem crossing (HISC), which can either compete with or surpass any other deactivation pathways, resulting in triplet-state population. (2) The rate of HISC is higher than that of the ISC at S_1 with lower vibrational energy (e.g., $v = 0$). It is noteworthy, herein, that the HISC processes in **1**−**6** may not be well-defined, rigorously speaking, because singlet and triplet states in the titled transition-metal complexes, to a certain extent, are mixed through spin−orbit coupling, as evidenced by the small but nonzero absorptivity for the lower-lying triplet states.[23] We nevertheless adopt this conventional terminology, i.e., singlet and triplet manifolds, for the convenience of the discussion throughout the context. Second, the term hyper is relative to the slower ISC at S_1 ($v = 0$) for the titled complexes only.

Bearing the mechanism in mind, we then made attempts to calculate the efficiencies of intersystem crossing and their corresponding rates at different excitation wavelengths from both steady state and dynamics approaches elaborated below.

Steady State Approaches: The Kinetics Analysis. To begin with, the efficiency of intersystem crossing at the highly electronically excited state S_n ($n > 1$) or vibrationally hot S_1 ($v > 0$), denoted as θ_{hisc}, is defined as the ratio for the rate of S_n (or S_1 ($v > 0$)) → T_m HISC versus the rate of the overall S_n (or S_1 ($v > 0$)) relaxation pathways. Starting from steady state approximation, the fluorescence quantum yield, Φ_f, is given by

$$\Phi_f = \frac{k_f}{k_f + k_{nr} + k_{isc}} \tag{1}$$

where k_f and k_{isc} are the radiative decay and intersystem crossing rate constants, respectively, and k_{nr} is the sum of all nonradiative decay rate constants except for k_{isc} when excited precisely to the lowest-lying S_1 state (λ_{ex} = 400 nm for **1**−**4** and 390 nm for **5**−**6**) near the absorption onset. Upon initially population to S_n states ($n > 1$) or the vibrationally excited S_1 state ($v > 0$), which is 266−380 nm excitation for the titled complexes, the observed fluorescence quantum yield, Φ_f^*, is defined as

$$\Phi_f^* = \frac{k_{ic}}{k_{ic} + k_{nr}^* + k_{hisc}} \cdot \Phi_f = \theta_{ic} \cdot \Phi_f \tag{2}$$

where k_{ic} is the rate of internal conversion (IC), which is coupled with vibrational relaxation (VR), to S_1 ($v = 0$). k_{hisc} is the intersystem rate constant at the S_n state. k_{nr}^* is the rate of any other deactivating pathways except for k_{ic} and k_{hisc}. Thus, the quantum efficiency of IC is given by

$$\theta_{ic} = \frac{\Phi_f^*}{\Phi_f} \tag{3}$$

Similarly, applying steady state approximation to the T_1 state renders the phosphorescence quantum yield

$$\Phi_p = \frac{k_{isc}}{k_f + k_{nr} + k_{isc}} \cdot \frac{k_p}{k_p + {}^3k_{nr}} = \theta_{isc} \cdot \theta_p \tag{4}$$

where θ_p represents the quantum efficiencies of phosphorescence, and θ_{isc} is defined as the quantum efficiency of intersystem crossing from S_1 ($v = 0$) to T_m. Furthermore, if we consider both S_n/S_1 ($v > 0$) → T_m → T_1 and S_n → S_1 → T_1 to evaluate the phosphorescence quantum yield after excitation to S_n

$$\Phi_p^* = \left(\frac{k_{hisc}}{k_{ic} + k_{nr}^* + k_{hisc}} \cdot \frac{{}^3k_{ic}}{{}^3k_{ic} + {}^3k_{nr}^* + {}^3k_{hisc}} + \theta_{ic} \cdot \theta_{isc} \right) \cdot \theta_p = (\theta_{hisc} \cdot {}^3\theta_{ic} + \theta_{ic} \cdot \theta_{isc}) \cdot \theta_p \tag{5}$$

where ${}^3k_{hisc}$ is the rate of T_m → S_{n-k} ($k \geq 1$). For the convenience of our derivation, we set ${}^3\theta_{ic} \sim 1$. Accordingly, we have obtained the quantum efficiency of HISC as

$$\theta_{hisc} = \theta_{isc} \cdot \left(\frac{\Phi_p^*}{\Phi_p} - \frac{\Phi_f^*}{\Phi_f} \right) \tag{6}$$

Except for θ_{isc}, all other parameters can be obtained from steady state spectra (Table 1). Fortunately, the absolute θ_{isc} value can be measured with a time-resolved thermal lensing (TRTL)[24] experiment (details of the TRTL setup and data analyses are elaborated in the Supporting Information) upon excitation near the onset of the S_0 ($v = 0$) → S_1 ($v = 0$) transition (e.g., 400 nm for **1**). As a result, θ_{isc} is measured to be 0.26 in degassed CH_2Cl_2 at 298 K for complex **1**. Accordingly, Figure 4 depicts the plot of θ_{hisc} as a function of excitation

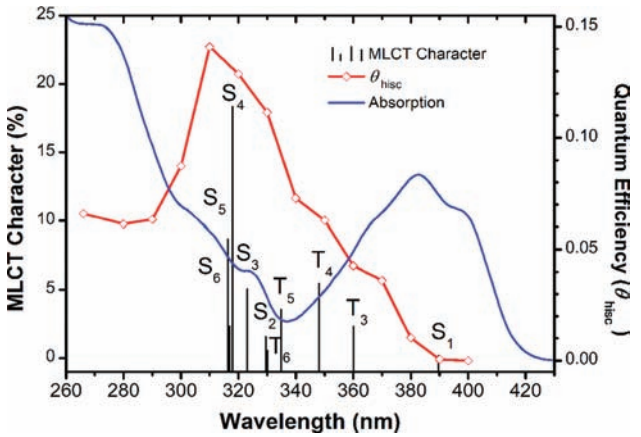

Figure 4. Right *y*-axis: The calculated θ_{hisc} at different λ_{ex} (−◇−). Left *y*-axis: the absolute value for computed percentage of MLCT character in absolute value for S_1−S_6 and T_3−T_5 (depicted in vertical solid black lines) of complex **1**. Notice that the absorption profile of complex **1** is also presented as a blue solid line for the reference.

wavelength. A drastic increase in θ_{hisc} from 0 at λ_{ex} = 400 nm to 0.14 at $\lambda_{ex} \sim 310$ nm is apparent, followed by a notable decline at $\lambda_{ex} < 310$ nm. These data will be used, together with the dynamics approach elaborated in the following section, to support the proposed mechanism.

Time-Resolved Studies: The Dynamics Measurement. *S_0 → S_1 Transition.* To gain in-depth insight into this anomalous phenomenon, relaxation dynamics in the femto−picosecond region was then inspected. The main focus of this work is on time-resolving the formation of the singlet excited states and their evolution to the lower-lying triplet states with transient absorption pump−probe spectroscopy. Upon excitation near the onset of the S_0 → S_1 transition (e.g., ∼400 nm), the difference optical spectra of representative complex 1 in CH_2Cl_2 as a function of time delays Δt (see Figure 5A) show salient spectral changes in the region of 450−720 nm: a broad-band absorption signal begins to evolve at λ_{max} = 625 nm near Δt = 0.5 ps, exhibiting blue shift and changes in spectral profile

dx.doi.org/10.1021/ja2107788 | J. Am. Chem. Soc. 2012, 134, 7715−7724

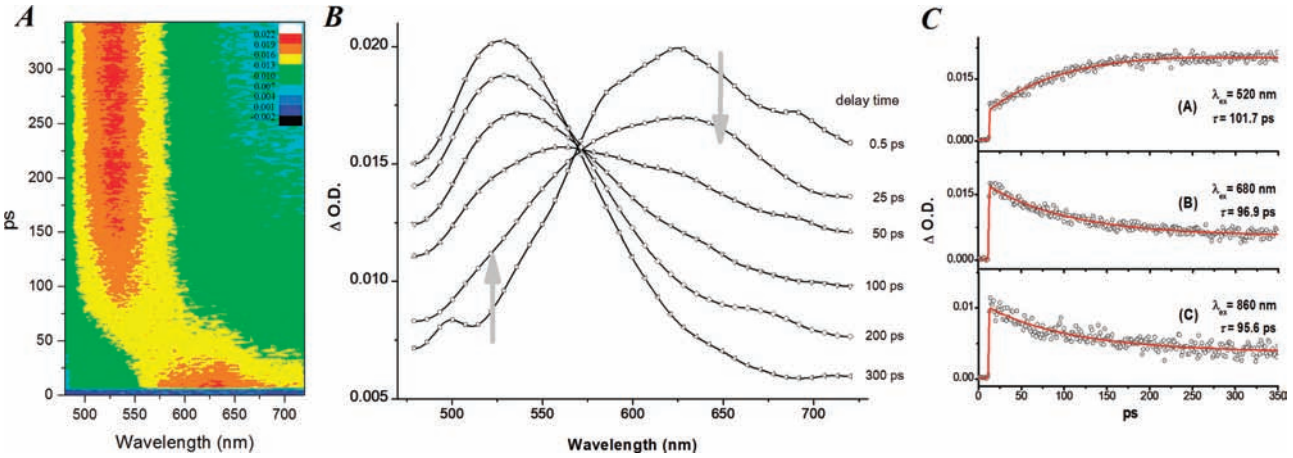

Figure 5. Femto–picosecond time-resolved transient absorption spectra for complex **1** in aerated CH_2Cl_2 solution at 298 K. (A) 2D mapping of the transient absorption spectra upon ~150 fs excitation at 400 nm. (B) Superimposed absorption difference spectra (in optical density, O.D.) at various delayed times, revealing an isosbestic point at λ = 570 nm. The acquisition time relative to the excitation pulse (Δt) is given at the right side of the spectra. (C) Single wavelength kinetics, with the probe wavelengths indicated on each figure. The solid lines through the data points correspond to biexponential fits of the data (circles) with time constants $\tau_1 \approx 100$ ps and $\tau_2 \approx 1$ μs.

until $\Delta t \sim 300$ ps, after which spectral evolution ceases. The resulting spectrum, maximized at ~520 nm, remains constant in intensity during the entire pump–probe delay time of 1000 ps. As shown in Figure 5B, the superposition of all acquired spectra reveals a prominent isosbestic point at λ = 570 nm. Single-wavelength kinetics curves are depicted in Figure 5C. Upon monitoring at 520 nm, the transient consists of an exponential rise component with a time constant of 101.7 ± 0.5 ps, which, within experimental error, is consistent with the decay component of 96.9 ± 0.3 and 95.6 ± 0.5 ps monitored at 680 and 860 nm, respectively.

Because an excitation wavelength of 400 nm approaches the onset of the $S_0 \rightarrow S_1$ transition for complex **1**, it is reasonable to assign the transient absorption centered around 625 nm with a decay time of ~100 ps to the $S_1 \rightarrow S_n$ ($n > 1$) transition and the 520 nm band with a much longer life span (≫1 ns) to the $T_1 \rightarrow T_m$ ($m > 1$) transition. The former assignment is confirmed by 1 kHz time-correlated single-photon counting (TCSPC) measurements monitoring at 440 nm fluorescence (Figure 6A) and the latter by the nanosecond transient absorption spectra elaborated in Figure 6B, in which a transient absorption band maximized at ~500 nm is revealed, having a spectral profile nearly identical to that acquired in femto–picosecond measurements after 300 ps. In the nanosecond measurements, the triplet–triplet transient absorption undergoes a first-order decay of $\tau \sim 0.82$ μs, consistent with the phosphorescence decay (~0.85 μs) of **1** in aerated CH_2Cl_2. In the femto–picosecond transient absorption shown in Figure 5C, also noted is the instantaneous absorption signal at, e.g., 520 nm, which is due to the overlapping $S_1 \rightarrow S_n$ band. In brief, with the isosbestic point observed at 570 nm and identical decay (625 nm band) and rise (520 nm band) dynamics, it is thus unambiguous to conclude that there is a precursor (625 nm band, S_1) to successor (520 nm band, T_1) relation between the two states. Furthermore, knowing the decay time of S_1 (~100 ps) and θ_{isc} = 0.26 (vide supra), the rate of S_1 (v = 0) intersystem crossing is then deduced to be 2.65×10^9 s^{-1}, which is more than 2 orders of magnitude slower than recent reports on Ru(II), Re(I), Fe(II), and Ir(III) complexes.[25−34] Nonetheless, observation of residual fluorescence in steady state measurements in combination with the correlation of dynamical features firmly supports that the slow ISC originates from the S_1 state.

$S_0 \rightarrow S_n$ Transition. Difference spectra measurements were also performed with high-energy excitation at 266 nm. The

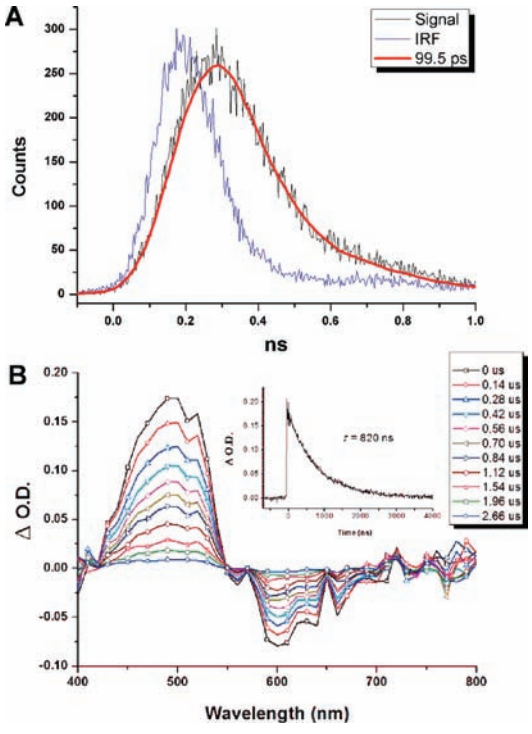

Figure 6. (A) 1 kHz TCSPC relaxation dynamics of complex **1** with 400 nm excitation. Black, blue, and red lines indicate the fluorescence decay monitored at 440 nm, instrumental response function, and best-fitting curve, respectively. (B) Nanosecond transient absorption spectra for **1** at different delay times. The single wavelength curve (probed at 490 nm) is fitted with an exponential decay time constant of 820 ns. Solution: aerated CH_2Cl_2. Temperature: 298 K. Notice that the negative absorption change is attributed to the stimulated phosphorescence, which is much more prominent in the nanosecond transient absorption and interferes with $T_1 \rightarrow T_m$ absorption so that the λ_{max} of $T_1 \rightarrow T_m$ absorption is at 500 nm instead of 520 nm.

dx.doi.org/10.1021/ja2107788 | J. Am. Chem. Soc. 2012, 134, 7715–7724

results for complex **1** (Figure 7A) display a broad absorption band with λ_{max} = 520 nm at each Δt and some other featureless

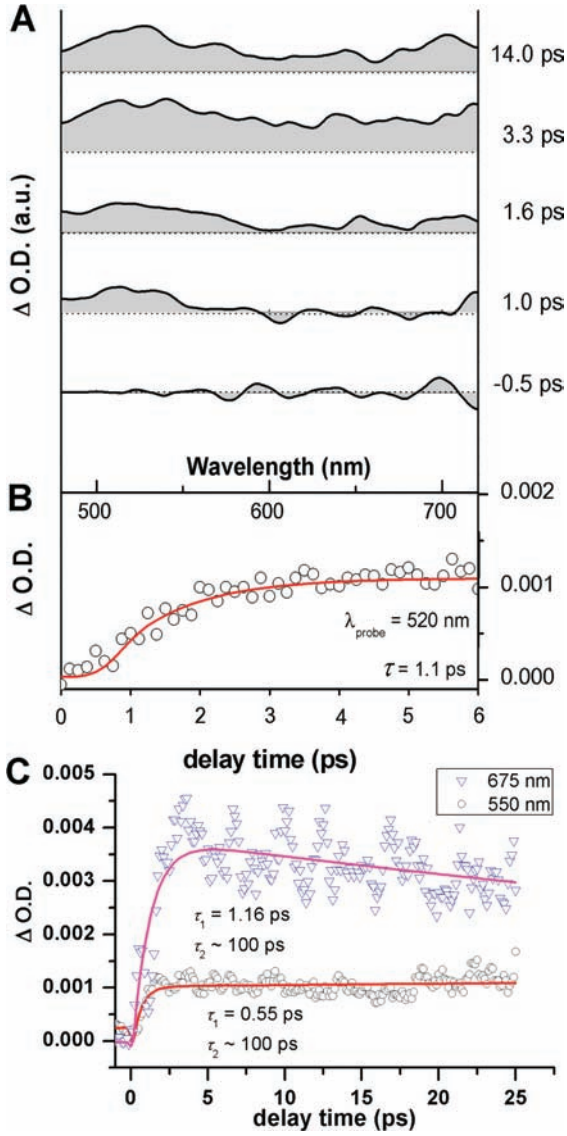

Figure 7. (A) Transient absorption spectra recorded upon 266 nm excitation. (B) The time trace at a probe wavelength of 520 nm. The solid line corresponds to an exponential fit to the data with a rise time of τ = 1.1 ps. (C) Early single wavelength kinetics at 550 nm ($T_1 \rightarrow T_m$) and 675 nm ($S_1 \rightarrow S_n$) upon 350 nm excitation. The solid lines correspond to three exponential fits of the data with $\tau_2 \approx 100$ ps and $\tau_3 \approx 1$ μs. Values in parentheses are the normalized amplitudes of the respective components.

bands without stationary λ_{max}. The $S_1 \rightarrow S_n$ absorption signal of λ_{max} = 625 nm is obscure, barely appearing within 0.5 ps after excitation by the 266 nm pump pulse. Nevertheless, the appearance of the $T_1 \rightarrow T_m$ absorption signal (λ_{max} = 520 nm) is obvious. The dynamics of triplet state formation is fast, as evidenced by its corresponding rise time constant of τ = 1.1 ps (see Figure 7B), which is approximately 2 orders of magnitude faster than that observed with 400 nm excitation (~100 ps). With the deduced θ_{hisc} of 0.068 at λ_{ex} = 266 nm, the rate constant of HISC is thus determined to be 6.2×10^{10} s^{-1}. Note that the late arrival of the transient absorption at $\lambda > 600$ nm is tentatively ascribed to the excited-state transition during internal conversion (IC) and/or vibrational relaxation (VR). Conventionally, upon excitation (e.g., 266 nm) to the highly excited states S_n, relaxation to S_1 is predominant via IC/VR processes in the condensed phase. Thus, on account of the prompt emergence of the triplet state absorption signal, as well as the data provided in steady state measurements (vide supra), a plausible explanation is that complex **1**, in certain higher-lying excited singlet states, undergoes fast intersystem crossing, the rate of which is either competitive to or even surpasses IC/VR processes. This rationalization holds true if the spin−orbit coupling matrix is large enough in that specific state.

Correlation between θ_{hisc} and MLCT. For the late transition metal complexes, recent empirical approaches have clearly established that electronic states directly involving metal (d_π or d_σ*) orbitals, such as the metal to ligand (π*) charge transfer (MLCT) state or vice versa (LMCT), should greatly enhance the rate of ISC.[23] Also, upon increasing the percentage of MLCT character, the rate of ISC increases accordingly.[35,36] In view of the titled complexes, which possess Os(II) d^6 configuration and octahedral coordination, we thus propose that the increase in the rate of intersystem crossing may correlate with increments of MLCT % in that specific excited state. Proof of this concept was provided with TD-DFT calculations, in which the B3LYP functional and a double-ζ quality basis set were used, consisting of Hay and Wadt's effective core potential (LANL2) for inner core electrons of the Os(II) atom, and a 6-31G* basis set for the rest of the atoms.[37] As a result, the first six electronic excited states in both singlet and triplet manifolds are evaluated, and the MLCT contribution can be assessed by MLCT(M%) = %(M)HOMO−x − %(M)LUMO+y, where %(M)HOMO−x and %(M)LUMO+y are electronic densities on the metal in HOMO−x and LUMO+y, respectively. If more than one single-electron excitation exists for a designated excited state, the expression is a sum of all charge transfer characters. Note that a similar approach is applied to obtain LMCT(M%) except that the value is negative. The plot of the sum of %MLCT and %LMCT (in absolute value) versus its corresponding states for, e.g., complex **1** is depicted in Figure 4, and pertinent numerical data are listed in Table S2 of Supporting Information. Qualitatively, the profile of the plot resembles that of the plot for θ_{hisc} as a function of excitation energy. For instance, the S_4 state, with an LMCT % of ~18%, is located at ~318 nm, which coincides with the maximum of θ_{hisc} (~14%) at 310 nm. Moreover, the S_1 state is contributed by as small as ~0.2% LMCT, manifesting its dominant $\pi\pi$* character and hence a much slower rate of ISC. From the viewpoint of chemical structure, complexes **1**−**6** are strategically designed by coordinating three mutually orthogonal CO ligands to the Os(II) center, such that the Os(II) d_π (t_g) energy, due to the enhanced Os(II) → CO back π-electron donation, is lower than the π orbitals of the anchored isoquinolinyl-triazolate/pyrazolate chromophore, which in turn become HOMO. To simplify the discussion, the relevant photophysical processes for **1**, together with each hypothetical potential energy surface, are qualitatively sketched in Figure 8, in which the rate of ISC, upon, e.g., 266 nm excitation, is designated to be within the same order as the rate of IC/VR (10^{11}−10^{12} s^{-1}) due to the appreciable %LMCT, while ISC with a much slower rate (10^9−10^{10} s^{-1}) is executed in the S_1 (v = 0) state. *That is, the efficiency of the T_1 population produced from the $S_1 \rightarrow T_1$ route is different from that of $S_n \rightarrow T_m \rightarrow T_1$, resulting in a remarkable excitation*

dx.doi.org/10.1021/ja2107788 | J. Am. Chem. Soc. 2012, 134, 7715−7724

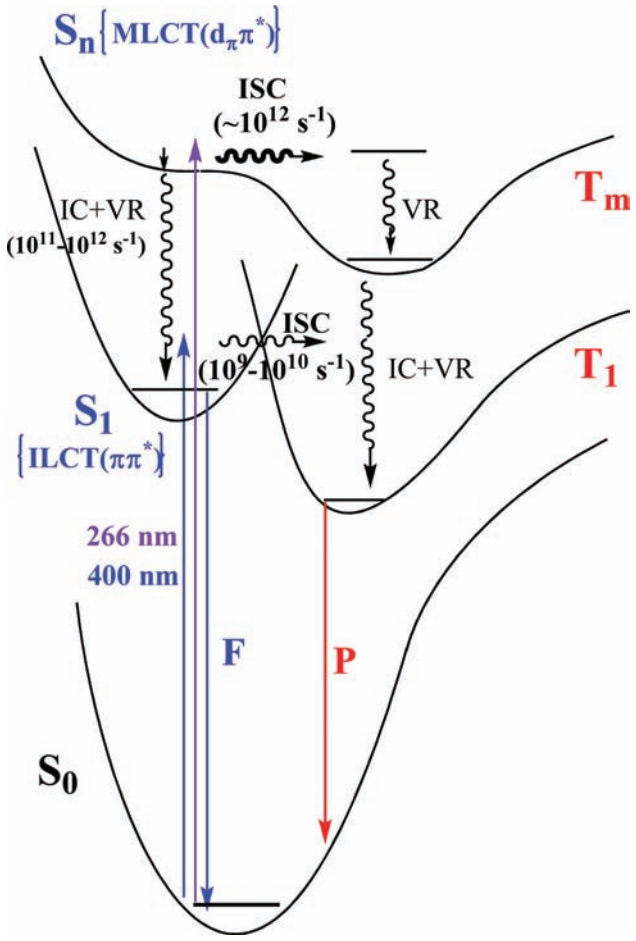

Figure 8. Proposed relaxation pathways and their time scales for the titled complexes **1**–**6**. F, fluorescence; P, phosphorescence. ISC, intersystem crossing; IC, internal conversion; VR, vibrational relaxation. Note that the subscript in each singlet (S) or triplet (T) manifold is nonspecific.

energy dependence in the intensity ratio for phosphorescence versus fluorescence.

Upon careful examination, we also notice a slight increase of θ_{hisc} in the range of 400–340 nm, for which the excitation energy is insufficient to reach S_2. The result can now be rationalized by the closely spaced triplet states, T_3–T_5 (Figure 4) in this region, resulting in $S_1 \rightarrow T_m$ HISC upon excitation to vibrationally hot S_1. This mechanism can be validated by transient absorption measurements taken with 350 nm excitation (Figure 7C). The kinetics obtained at 675 nm of the $S_1 \rightarrow S_n$ absorption band can be fitted with a 1.16 ps rise and a ~100 ps decay, which are approximately equal in amplitude. The fast rise is attributed to VR toward the thermally equilibrated S_1 state ($v = 0$). On the other hand, the $T_1 \rightarrow T_m$ signal at 550 nm can be fitted with two rise time constants, $\tau_1 = 0.55$ ps and $\tau_2 \approx 100$ ps. The difference in the two fast but finite τ_1 time constant implies that there are diverged ultrafast relaxation pathways following 350 nm excitation, including 1.16 ps VR at the S_1 state and the 0.55 ps T_1 state formation through S_1 ($v > 0$) $\rightarrow T_m \rightarrow T_1$. As an additional note, θ_{hisc} can thus be viewed as the fraction of T_1 generated via $S_n \rightarrow T_m \rightarrow T_1$ or S_1 ($v > 0$) $\rightarrow T_m \rightarrow T_1$. At $\lambda_{ex} <$ 310 nm, $\theta_{hisc} \sim \Phi_P^*$, indicating that the generation of T_1 is dominated by HISC instead of the commonly acknowledged S_1 ($v = 0$) $\rightarrow T_1$ ISC at high-energy excitation (see eq 5 with $\theta_p \sim 1$ determined by TRTL).

This proposed mechanism turns out to be well suited for other titled complexes. As shown in Table 1, investigation of the congeners of **1**, i.e., **2**–**6**, reveals similar excitation-wavelength-dependent ratiometric emission. Results of femto–picosecond transient absorption reveal that the time scales (<1.5 ps) of ISC for **2**–**6** (see Table 1) in the highly excited state (e.g., via 266 nm excitation) are all much faster than those of a few hundred picoseconds resolved in the S_1 state. This type of excitation-wavelength-dependent dual emission and ISC dynamics is remarkable and has not yet been recognized but should be universal to any transition-metal complexes possessing $\pi\pi^*$ as the lowest-lying transition. We have further proven this concept in yet another Os(II) complex **7**, which bears a β-diketonate chromophore (Chart 1),[15] as well as in a d^{10} Ag(I) complex **8**.[16] For these complexes, there will always be some higher excited states in which the percentage of metal d orbital involvement (either d_π or d_σ^*) is substantial such that faster ISC is executed. Evidently, this is also manifested in the steady state emission and excitation spectra (Figure 9). In other words, as the late transition metal

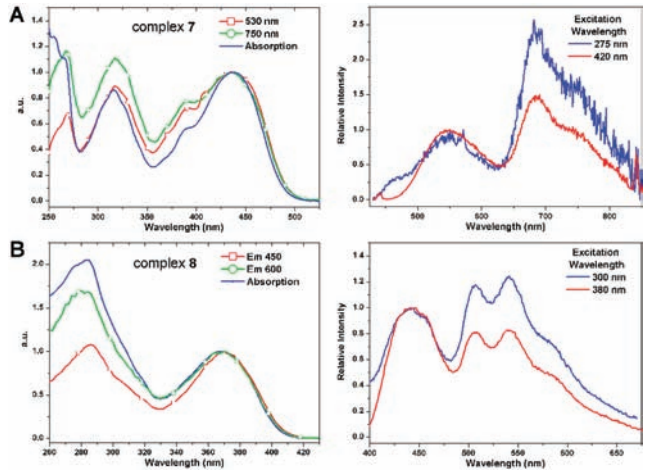

Figure 9. (A) Normalized absorption and excitation spectra at the indicated emission wavelengths of **7** and **8** in degassed CH_2Cl_2 at 298 K. (B) Excitation-wavelength-dependent emission spectra normalized at the fluorescence peak maxima.

complexes lack metal contribution in the S_1 state, whereas MLCT/LMCT is significant in higher-lying excited states, the population of the T_1 state can bypass S_1 via the $S_n \rightarrow T_m \rightarrow T_1$ process. Unambiguously, the system demonstrated here exhibits a purely photophysical phenomenon in which ISC is more emphasized at higher electronic excited states. Most importantly, had it not been for the unconventional ISC on the subnanosecond time scale at the S_1 state, the $S_n \rightarrow T_m \rightarrow T_1$ and $S_n \rightarrow S_1 \rightarrow T_1$ processes would both be ultrafast and impossible to differentiate. Intriguingly, nanosecond ISC rates have also been studied recently on complexes involving Rh and Au atoms.[38–40] Yet, we believe that this work is the first comprehensive investigation into the underlying mechanism for transition-metal complexes with anomalously slow ISC, which incorporates steady state measurements, ultrafast dynamics, and theoretical calculation. Moreover, the excitation-wavelength- or state-dependent behavior is explored herein for the first time.

dx.doi.org/10.1021/ja2107788 | J. Am. Chem. Soc. 2012, 134, 7715–7724

CONCLUSION AND PERSPECTIVE

Herein, using a series of newly designed Os(II) and Ag(I) complexes as the paradigm, we demonstrate unambiguously the harnessing of the triplet state via high electronically excited states. This mechanism of "harvesting triplet manifold", in theory, should be general and can be extended to organic molecules undergoing forbidden S_1 ($\pi\pi^*$) → T_1 ($\pi\pi^*$) ISC if certain highly electronic excited states are $n\pi^*$ in character (here n stands for the nonbonding orbital) and thus have a substantial amount of spin−orbit coupling matrix stemming from vibronic borrowing so that the S_n ($^1n\pi^*$) → T_m ($^3\pi\pi^*$) ISC is partially allowed.[41] In fact, such wavelength dependence has been found in diphenylpolyynes at critical bond numbers where the symmetries of electronic states switch.[42] Nevertheless, such a coupling matrix is much weaker than that induced by MLCT/LMCT transition discussed herein. Therefore, the rate of S_n → T_m ISC for typical organic molecules ought to be much less competitive versus IC/VR in the condensed phase.

The above mechanism of harvesting triplet state may have deep ramifications in view of applications. A readily accessible experiment is exemplified by the on/off switch for complex **1**, exploiting phosphorescence/fluorescence ratiometric changes between one- and two-photon processes upon 400 nm excitation (see Supporting Information Figure S3). As the excitation power is increased, the P/F ratio is enhanced, which is rationalized by some extent of two-photon excitation. An ideal photonic switch for one- versus two-photon excitation can thus be achieved by setting a threshold for the P/F ratio. Likewise, the concept renders such molecules essentially bifunctional if applied to bioimaging. For instance, with low-intensity (one-photon) excitation, these metal complexes act primarily as benign fluorescent agents. In contrast, with high-intensity (two-photon) excitation to higher excited states, the target molecules carry out photodynamic therapy[43] following accelerated triplet state population. We also consider applications over two imminent research fields: On the one hand, color-tunable OLED (organic light-emitting diode) devices for which the color of luminescence can be changed via altering the applied voltage may be fabricated,[44−46] such that the electron−hole recombination is accomplished in different excited states. Moreover, within the tuning range, white light emitting capability may be achieved in a single-layered manner.

In yet another perspective, it has been confirmed that the performance of photovoltaic cells differs between singlet and triplet electron injection routes.[47−50] In typical dye-sensitized solar cells (DSSCs) incorporating second- and third-row transition-metal complexes, electron injection into the conduction band of semiconductors such as TiO_2 proceeds predominantly from the long-lived triplet state formed within <1 ps. However, owing to the lower energy of the triplet state, the energetics is less favorable for electron injection, and hence the rate is slower than that for the singlet state. It would be interesting to analyze the net device efficiency and the wavelength-dependent incident photon-to-electron conversion efficiency (IPCE) spectrum for complexes with prolonged S_1 state lifetime.

In sum, for the titled transition metal complexes, when absorbing at the red end of the spectrum, the dominant $^1\pi\pi^*$ transition results primarily in singlet state population, whereas shorter wavelength excitation to higher-lying MLCT states leads to a higher ratio of triplet state, that is, "harvesting highly electronically excited energy to triplet states".

ASSOCIATED CONTENT

Supporting Information

(1) Excitation wavelength-dependent steady state emission spectra of complex **1** in degassed CH_2Cl_2, (2) solid-state photoluminescence spectra, (3) two-photon excitation fluorescence and phosphorescence spectra, (4) the experimental setup and the result of time-resolved thermal lensing, (5) absolute fluorescence and phosphorescence quantum yields, (6) calculated MLCT characters of lower-lying singlet and triplet states for complex **1**. This material is available free of charge via the Internet at http://pubs.acs.org.

AUTHOR INFORMATION

Corresponding Author

chop@ntu.edu.tw; ychi@mx.nthu.edu.tw

Present Address

[§]School of Applied Chemistry, Chung Shan Medical University, No.110, Sec. 1, Jianguo N. Rd., Taichung 40201, Taiwan, R.O.C.

Notes

The authors declare no competing financial interest.

ACKNOWLEDGMENTS

This work was funded by the National Science Council of Taiwan, ROC. We are also grateful to the National Center for High-Performance Computing for computer time and facilities.

REFERENCES

(1) Kasha, M. *Faraday Soc. Discuss* **1950**, *9*, 14−19.
(2) Polivka, T.; Sundström, V. *Chem. Rev.* **2004**, *104*, 2021−2072.
(3) Beer, M.; Longuet-Higgins, H. C. *J. Chem. Phys.* **1955**, *23*, 1390−1391.
(4) Oka, T.; Knight, A. R.; Steer, R. P. *J. Chem. Phys.* **1977**, *66*, 699−706.
(5) Cordes, T.; Malkmus, S.; DiGirolamo, J. A.; Lees, W. J.; Nenov, A.; de Vivie-Riedle, R.; Braun, M.; Zinth, W. *J. Phys. Chem. A* **2008**, *112*, 13364−13371.
(6) Baldo, M. A.; O'Brien, D. F.; You, Y.; Shoustikov, A.; Sibley, S.; Thompson, M. E.; Forrest, S. R. *Nature* **1998**, *395*, 151−154.
(7) Lamansky, S.; Djurovich, P.; Murphy, D.; Abdel-Razzaq, F.; Lee, H. E.; Adachi, C.; Burrows, P. E.; Forrest, S. R.; Thompson, M. E. *J. Am. Chem. Soc.* **2001**, *123*, 4304−4312.
(8) Endo, A.; Suzuki, K.; Yoshihara, T.; Tobita, S.; Yahiro, M.; Adachi, C. *Chem. Phys. Lett.* **2008**, *460*, 155−157.
(9) Minaev, B.; Agren, H.; De Angelis, F. *Chem. Phys.* **2009**, *358*, 245−257.
(10) O'Regan, B.; Gratzel, M. *Nature* **1991**, *353*, 737−740.
(11) Grätzel, M. *Inorg. Chem.* **2005**, *44*, 6841−6851.
(12) Deeming, A. J.; Meah, M. N.; Randle, N. P.; Hardcastle, K. I. *J. Chem. Soc., Dalton Trans.* **1989**, *11*, 2211−2216.
(13) Deeming, A. J.; Randle, N. P.; Bates, P. A.; Hursthouse, M. B. *J. Chem. Soc., Dalton Trans.* **1988**, *11*, 2753−2757.
(14) Tung, Y. L.; Chen, L. S.; Chi, Y.; Chou, P. T.; Cheng, Y. M.; Li, E. Y.; Lee, G. H.; Shu, C. F.; Wu, T. I.; Carty, A. *J. Adv. Funct. Mater.* **2006**, *16*, 1615−1626.
(15) Chen, Y. L.; Li, S. W.; Chi, Y.; Cheng, Y. M.; Pu, S. C.; Yeh, Y. S.; Chou, P. T. *ChemPhysChem* **2005**, *6*, 2012−2017.
(16) Hsu, C.-W.; Lin, C.-C.; Chung, M.-W.; Chi, Y.; Lee, G.-H.; Chou, P.-T.; Chang, C.-H.; Chen, P.-Y. *J. Am. Chem. Soc.* **2011**, *133*, 12085−12099.
(17) Hsieh, C. C.; Chou, P. T.; Shih, C. W.; Chuang, W. T.; Chung, M. W.; Lee, J.; Joo, T. *J. Am. Chem. Soc.* **2011**, *133*, 2932−2943.

(18) Becke, A. D. *J. Chem. Phys.* **1993**, *98*, 5648−5652.
(19) Ditchfield, R.; Hehre, W. J.; Pople, J. A. *J. Chem. Phys.* **1971**, *54*, 724−728.
(20) Hay, P. J.; Wadt, W. R. *J. Chem. Phys.* **1985**, *82*, 270−283.
(21) Stratmann, R. E.; Scuseria, G. E.; Frisch, M. J. *J. Chem. Phys.* **1998**, *109*, 8218−8224.
(22) Záliš, S.; Ben Amor, N.; Daniel, C. *Inorg. Chem.* **2004**, *43*, 7978−7985.
(23) Chou, P.-T.; Chi, Y.; Chung, M.-W.; Lin, C.-C. *Coord. Chem. Rev.* **2011**, *255*, 2653−2665.
(24) Twarowski, A. J.; Kliger, D. S. *Chem. Phys.* **1977**, *20*, 253−258.
(25) Damrauer, N. H.; Cerullo, G.; Yeh, A.; Boussie, T. R.; Shank, C. V.; McCusker, J. K. *Science* **1997**, *275*, 54−56.
(26) Yeh, A. T.; Shank, C. V.; McCusker, J. K. *Science* **2000**, *289*, 935−937.
(27) McCusker, J. K. *Acc. Chem. Res.* **2003**, *36*, 876−887.
(28) Juban, E. A.; McCusker, J. K. *J. Am. Chem. Soc.* **2005**, *127*, 6857−6865.
(29) Cannizzo, A.; Blanco-Rodriguez, A. M.; El Nahhas, A.; Sebera, J.; Záliš, S.; Vlcek, A.; Chergui, M. *J. Am. Chem. Soc.* **2008**, *130*, 8967−8974.
(30) El Nahhas, A.; Consani, C.; Blanco-Rodriguez, A. M.; Lancaster, K. M.; Braem, O.; Cannizzo, A.; Towrie, M.; Clark, I. P.; Záliš, S.; Chergui, M.; Vlcek, A. *Inorg. Chem.* **2011**, *50*, 2932−2943.
(31) Consani, C.; Premont-Schwarz, M.; ElNahhas, A.; Bressler, C.; van Mourik, F.; Cannizzo, A.; Chergui, M. *Angew. Chem., Int. Ed.* **2009**, *48*, 7184−7187.
(32) Gawelda, W.; Cannizzo, A.; Pham, V. T.; van Mourik, F.; Bressler, C.; Chergui, M. *J. Am. Chem. Soc.* **2007**, *129*, 8199−8206.
(33) Hedley, G. J.; Ruseckas, A.; Samuel, I. D. W. *J. Phys. Chem. A* **2009**, *113*, 2−4.
(34) Hedley, G. J.; Ruseckas, A.; Samuel, I. D. W. *Chem. Phys. Lett.* **2008**, *450*, 292−296.
(35) Chou, P. T.; Chi, Y. *Chem.—Eur. J.* **2007**, *13*, 380−395.
(36) Chi, Y.; Chou, P. T. *Chem. Soc. Rev.* **2007**, *36*, 1421−1431.
(37) Hwang, K. C.; Chen, J. L.; Chi, Y.; Lin, C. W.; Cheng, Y. M.; Lee, G. H.; Chou, P. T.; Lin, S. Y.; Shu, C. F. *Inorg. Chem.* **2008**, *47*, 3307−3317.
(38) Steffen, A.; Tay, M. G.; Batsanov, A. S.; Howard, J. A. K.; Beeby, A.; Vuong, K. Q.; Sun, X. Z.; George, M. W.; Marder, T. B. *Angew. Chem., Int. Ed.* **2010**, *49*, 2349−2353.
(39) Tong, G. S. M.; Chow, P. K.; Che, C. M. *Angew. Chem., Int. Ed.* **2010**, *49*, 9206−9209.
(40) Lu, W.; Kwok, W.-M.; Ma, C.; Chan, C. T.-L.; Zhu, M.-X.; Che, C.-M. *J. Am. Chem. Soc.* **2011**, *133*, 14120−14135.
(41) El-Sayed, M. A.; Tinti, D. S.; Owens, D. V. *Chem. Phys. Lett.* **1969**, *3*, 339−342.
(42) Nagano, Y.; Ikoma, T.; Akiyama, K.; Tero-Kubota, S. *J. Am. Chem. Soc.* **2003**, *125*, 14103−14112.
(43) Pawlicki, M.; Collins, H. A.; Denning, R. G.; Anderson, H. L. *Angew. Chem., Int. Ed.* **2009**, *48*, 3244−3266.
(44) Welter, S.; Brunner, K.; Hofstraat, J. W.; De Cola, L. *Nature* **2003**, *421*, 54−57.
(45) Reyes, R.; Cremona, M.; Teotonio, E. E. S.; Brito, H. F.; Malta, O. L. *Chem. Phys. Lett.* **2004**, *396*, 54−58.
(46) Jou, J. H.; Wu, M. H.; Shen, S. M.; Wang, H. C.; Chen, S. Z.; Chen, S. H.; Lin, C. R.; Hsieh, Y. L. *Appl. Phys. Lett.* **2009**, *95*, 013307.
(47) Penny, M.; Farrell, T.; Please, C. *Sol. Energy Mater. Sol. Cells* **2008**, *92*, 11−23.
(48) Koops, S. E.; O'Regan, B. C.; Barnes, P. R. F.; Durrant, J. R. *J. Am. Chem. Soc.* **2009**, *131*, 4808−4818.
(49) Benkö, G.; Kallioinen, J.; Korppi-Tommola, J. E. I.; Yartsev, A. P.; Sundström, V. *J. Am. Chem. Soc.* **2002**, *124*, 489−493.
(50) Katoh, R.; Furube, A.; Kasuya, M.; Fuke, N.; Koide, N.; Han, L. *J. Mater. Chem.* **2007**, *17*, 3190−3196.